Article



Observation of Analogue Dynamic Schwinger Effect and Non-Perturbative Light Sensing in Lead Halide Perovskites

Dusan Lorenc, Artem G. Volosniev,*, Ayan A. Zhumekenov, Seungho Lee, Maria Ibáñez, Osman M. Bakr, Mikhail Lemeshko, and Zhanybek Alpichshev*



Cite This: ACS Photonics 2025, 12, 5220-5230



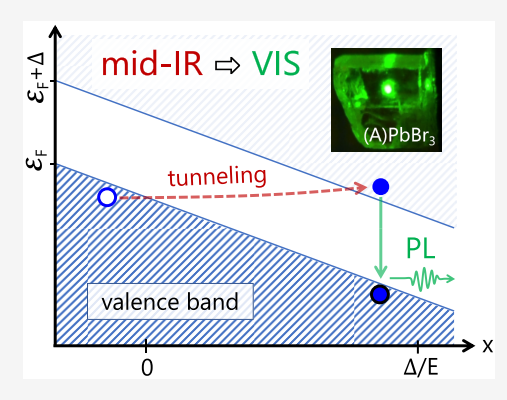
ACCESS I

III Metrics & More

Article Recommendations

Supporting Information

ABSTRACT: Dielectric breakdown of physical vacuum (Schwinger effect) is the textbook demonstration of compatibility of Relativity and Quantum theory. Although observing this effect is still practically unachievable, its analogue generalizations have been shown to be more readily attainable. This paper demonstrates that a gapped Dirac semiconductor, methylammonium lead-bromide perovskite (MAPbBr₃), exhibits analogue dynamic Schwinger effect. Tunneling ionization under deep subgap mid-infrared irradiation leads to intense photoluminescence in the visible range, in full agreement with quasi-adiabatic theory. In addition to revealing a gapped extended system suitable for studying the analogue Schwinger effect, this observation holds great potential for nonperturbative field sensing, i.e., sensing electric fields through nonperturbative light-matter interactions. First, this paper illustrates this by measuring the local deviation from the nominally cubic phase of a perovskite single crystal, which can be



interpreted in terms of frozen-in fields. Next, it is shown that analogue dynamic Schwinger effect can be used for nonperturbative amplification of nonparametric upconversion process in perovskites driven simultaneously by multiple optical fields. This discovery demonstrates the potential for material response beyond perturbation theory in the tunneling regime, offering extremely sensitive light detection and amplification across an ultrabroad spectral range not accessible by conventional devices.

KEYWORDS: photoluminescence, quasi-adiabatic tunneling ionization, Dirac equation, Landau-Dykhne approximation, electric field detection

■ INTRODUCTION

One of the most important insights coming from the synthesis of Quantum Mechanics and Special Relativity is the realization that vacuum is not empty. Instead, it is rather a fluctuating sea of virtual particle-antiparticle pairs, which can be in principle made real in the presence of external fields. However, this process is negligible unless the fields are of the order of $E_{\rm S} \approx$ 10¹⁸ V/m at which point particle-antiparticle creation leads to the dielectric breakdown of vacuum. In view of the enormity of $E_{\rm S}$ and its intuitive interpretation as the maximal static electric field attainable in principle, it is natural that the actual attempts to realize vacuum breakdown ("Schwinger Effect", SE) focus on its dynamical versions where the vacuum pair creation is achieved under the influence of time-dependent fields,² which are easier to create (from a modern technological point of view) than the static ones. To further facilitate the observation of SE, theoretical studies suggest either to increase the frequency of the driving field^{3,4} or to tailor the driving field profiles.^{5,6} However, any theoretical proposal must rely on certain simplifying assumptions, which due to the inherently nonperturbative character of SE may be decisive to the outcome.⁷⁻⁹ Given that current technology is not capable to

test these ideas in practice, it is hard to tell at the moment how realistic will they ultimately turn out to be.

In this context it appears desirable to be able to simulate the Schwinger effect and the various approaches to it in more accessible settings, such as cold-atom quantum simulators or semiconductors. As the connection between the Landau-Zener transition 17,18 and the Schwinger effect is well understood (see, e.g., ref 19), arguably, the most theoretically explored simulator is a semiconductor with a gapped Dirac-like band dispersion. ^{13,16} It is straightforward to demonstrate then that the threshold field in this case would be $E_{\rm s} \sim \Delta/ea \sim 10^8 {\rm V/m}$, which is readily achievable in modern laboratories (here Δ , a and e are the band gap, unit lattice length and the elementary charge, respectively). However, it turns out that the observation of this scaled-down version of SE also poses significant challenges. The main difficulty here

Received: June 12, 2025 Revised: July 23, 2025 Accepted: July 23, 2025 Published: August 11, 2025





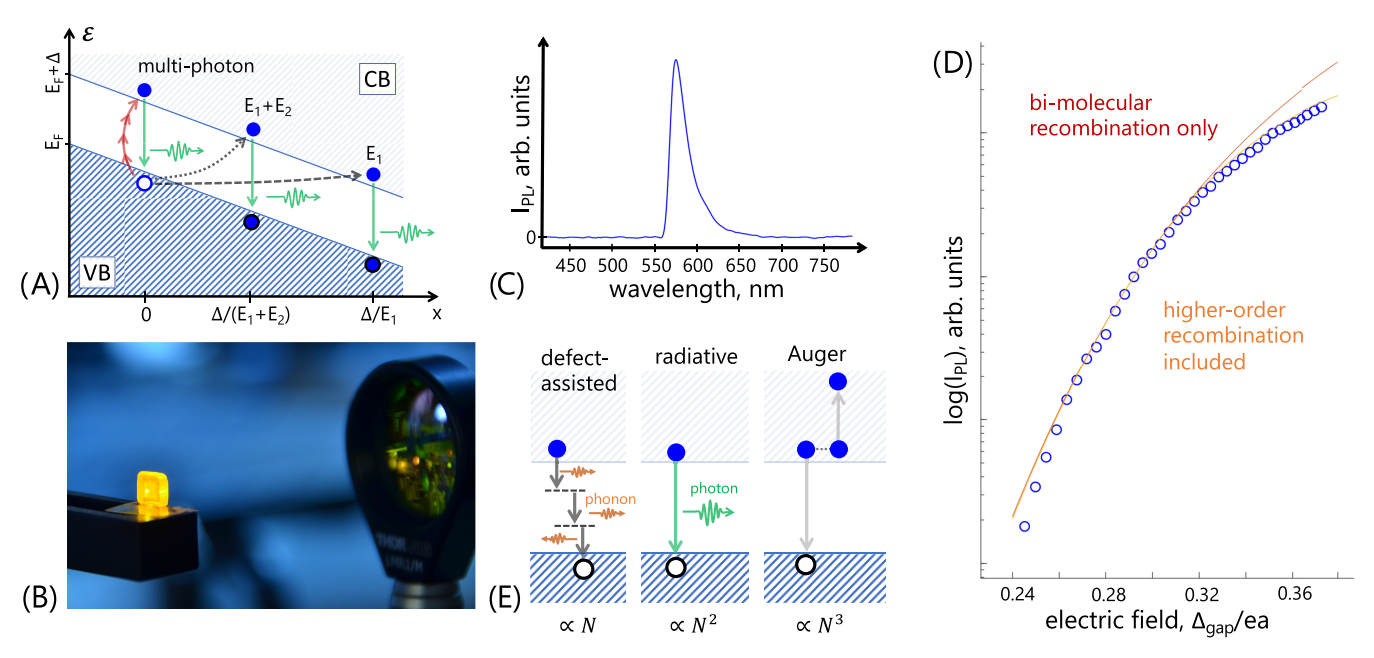


Figure 1. (A) Schematic diagram of ionization across the energy gap Δ due to multiphoton process, and due to tunneling under the influence of different applied field amplitudes (E_1 and $E_1 + E_2$). It can be seen that the magnitude of E determines the width of the forbidden range, thus affecting the net tunneling rate exponentially (see the text for details); (B) MAPbBr₃ crystal with PL coming from the bulk of the sample; (C) PL spectrum of MAPbBr₃ single crystal sample pumped by $\lambda = 4 \mu \text{m}$ radiation; (D) PL spectra of MAPbBr₃ single crystal sample under $\lambda = 4 \mu \text{m}$ pumping, together with our theoretical prediction for weak and intermediate electric fields (see the main text and Methods for details); (E) An illustration of several common channels of photocarrier recombination with characteristic rate dependencies on the density of charge carriers, n.

lies in the fact that despite an abundance of far-reaching analogies, 20,21 there is an important difference between the "true" Dirac field in vacuum and a Dirac material in that the former features relativistic invariance while the latter does not. The important consequence in question is that a free particle in vacuum can in principle be accelerated indefinitely, while a charge carrier in a semiconductor can produce secondary particles once it acquires a certain threshold kinetic energy comparable to the band gap.²² Since the threshold for this process $E_{\rm av}\sim \Delta/e\lambda_{\rm mfp}$ is significantly lower than that for tunneling ionization (here $\lambda_{\rm mfp}>a$ is the mean free path of charged carriers in the material), the population of secondary charge carriers will tend to dominate over tunnel-ionized carriers, often ending up in a catastrophic avalanche breakdown of the material. As a result of these complications, the observations of tunneling ionization have been limited so far either to the cases where the relevant tunneling region is restricted to a narrow part of space to avoid avalanche breakdown (e.g., tunneling ionization in single atoms, ²³ in a spatially localized graphene junction²⁴ or tunnel diodes²⁵ and tunnel junctions^{26,27} in electronics); or to extended systems with no gap.²⁸ However, to draw a direct analogy with highenergy physics, it is essential to identify materials and conditions that enable the realization of a Schwinger-like effect in an extended Dirac material with a finite bandgap. Note that in this work, 'Dirac material' refers to a system whose underlying Hamiltonian exhibits a Dirac-like spinmomentum coupling and a particle-antiparticle structure. This definition, which is standard nowadays, 20 refines early works based upon a Dirac-like energy-momentum relation.²¹]

In this Article, we report the observation of dynamical tunneling ionization in a single-crystal sample of lead halide perovskite (LHP), which realizes a gapped Dirac system.²⁹ In order to suppress avalanche formation and emphasize

tunneling, we note that the former needs a finite amount of time to build up while the latter occurs quasi-instantaneously. Therefore, we seek to induce ionization with alternating electric fields using frequencies that, on the one hand, correspond to photon energies significantly smaller than the band gap $\hbar\omega\ll\Delta$ (to ensure that we operate in the quasiadiabatic regime); on the other hand, they should oscillate fast enough to avoid an avalanche breakdown ($\omega \gtrsim eE/\sqrt{m\Delta}$, where E and m are the magnitude of the applied electric field and the band mass of the charge carrier, respectively). Additionally, we are careful to keep our irradiation intensity levels well below impact ionization thresholds for our pulse durations $\tau \approx 300$ fs to suppress the population of secondary charge carriers.³⁰ Operation with relatively small intensities also allows us to avoid 'memory' effects in our system, which are extrinsic to tunneling ionization (see Supporting Information). This is necessary to reveal the tunneling processes inherent in the material and also to be able to describe them using quasi-adiabatic methods.

Low irradiation intensities, however, imply that all measurements need to be performed in the regime where the concentration of tunnel-induced carriers is so low that standard transport measurements cannot be used for studying tunnel ionization. Therefore, our approach here is to infer the population of photoexcited carriers from the intensity of photoluminescence (PL) emitted upon their recombination with each other. The success of this approach crucially depends on two factors. First, the energy gap of the material should be free of defects to enhance the probability of tunneling directly into the conduction band. Second, the parent material should enjoy high photoluminescence quantum efficiency, namely the ratio of radiative recombinations to the total number of excitations.³¹ These considerations are the primary motivation for the choice of lead halide perovskites as the base for

realizing the solid-state version of SE.³² Furthermore, effective behavior of lead halide perovskites renowned for excellent quantum optoelectronic properties³³ is described very accurately by a Dirac equation with a nonzero mass, ^{34–36} strengthening the analogy between our findings and the physics of SE.

Beyond fueling interest in basic strong-field physics discussed at the beginning of the paper, the observed tunneling ionization offers a promising avenue for sensitive electric field detection, even in the regimes where conventional sensors encounter limitations. To explore this avenue, we leverage the exponential dependence of tunneling ionization on electric field strength in the second part of the paper. Lead-halide perovskites appear as advantageous sensing materials, as the key characteristics of tunneling ionization remain robust with respect to variations in chemical/physical composition of the sample. To substantiate this claim, we will briefly discuss an alternative lead-halide perovskite, CsPbBr₃ (see Supporting Information and ref 37), as well as dust-like perovskite samples.

■ OBSERVATION OF TUNNELING IONIZATION IN MAPbBr₃

Lead-halide perovskites are known to feature strong subbandgap response in terms of two- and three-photon absorption^{38,39} whose analysis has been mainly focused around the photophysical properties of LHPs in the near-infrared regime as it can shed light onto surprising solar cell (photovoltaic) performance of LHPs. 40 At the same time, the response of the system to photons with lower frequency remains largely unexplored. In Figure 1C we show the PL spectrum of single-crystal MAPbBr3 illuminated with midinfrared radiation ($\lambda \approx 4 \mu m$), see Experimental section for further details. Given the wavelength of PL ($\lambda_{PL} \approx 570 \text{ nm}$) which roughly corresponds to the bandgap energy in MAPbBr₃ $(\Delta \approx 2.4 \text{ eV}^{41,42})$ this process corresponds to a whopping frequency conversion factor of ~ 10 at the face value. Combined with the exponential sensitivity of this process to the intensity of the irradiating field in Figure 1D, we are compelled to rationalize the observed PL under deep subgap irradiation as quasi-adiabatic tunnel ionization of electrons across the semiconductor band gap using the standard terminology of strong-field phenomena 43 (similar behavior was observed in CsPbBr₃, which indicates the general character of the phenomenon; see Supporting Information and ref 37). This observation comprises the central finding of this work. In the following we will further substantiate this qualitative observation by a comprehensive quantitative analysis of ionization in a periodically driven Dirac-like band structure.

Quasi-Adiabatic Tunneling. Tunneling is the quintessential quantum effect whereby a system undergoes a transition that can be described semiclassically by a trajectory of which at least a part passes through a classically forbidden region in the parameter space. As a result the rate of this transition is strongly suppressed, being exponentially sensitive to the width of the classically forbidden region, ⁴⁴ see Figure 1A. For instance, in a static electric field, E, the rate of tunneling ionization W across the gap Δ can be shown to be

$$W \propto \exp(-E_{\rm s}/|E|) \tag{1}$$

with the characteristic cutoff field introduced above $E_{\rm s} \sim \Delta/ea.^{1,17,18}$ In the original Schwinger work, the energy and length scales appear from the Dirac equation: $2m_{\rm e}c^2$ as the gap

and the reduced Compton wavelength $\lambda_{\rm C} = \hbar/(m_{\rm e}c)$ in place of a, which leads to $E_{\rm S} = m_{\rm e}c^2/(e\lambda_{\rm C})$; here m_e is the mass of an electron and c is the speed of light. The huge disparity between these energy scales and those typical in semiconductor physics brings the observation of the analogue Schwinger effect significantly closer to experimental realization.

A convenient way to extend the expression in eq 1 to the problem of tunneling excitation of a semiconductor under the influence of time-dependent fields varying at the characteristic frequencies much smaller than those given by the bandgap is the so-called quasi-adiabatic Landau-Dykhne method. Within this approach the ionization rate W can be shown (see Methods) to be given as

$$W \sim \exp(-2f(\gamma_{\rm K})\Delta/\omega) \tag{2}$$

where $f(x) = \operatorname{arsinh}(x) - (\sinh(2\operatorname{arsinh}(x)) - 2\operatorname{arsinh}(x))/(8x^2)$, and γ_K is the so-called Keldysh parameter of the problem whose numeric value depends on the strength and the frequency of the driving field as well as on the details of the band structure of the material in question. In the specific case of lead-bromide perovskites, density functional theory calculations provide $\gamma_K \simeq 0.85 \ \hbar \omega/(eaE_{AC})$, where E_{AC} is the strength of the electric field induced by the laser, and $a \simeq 0.586$ nm is the lattice constant MAPbBr₃ in cubic phase. In the specific case

The value of the Keldysh parameter determines the degree of adiabaticity of the problem, the two limiting cases being pure adiabatic tunneling ($\gamma_{\rm K} \to 0$) and multiphoton absorption ($\gamma_{\rm K} \to \infty$) as illustrated in Figure 1A. Using the known ${\bf k}\cdot{\bf p}$ parameters of MAPbBr3 in cubic phase, we calculate in the limit $\gamma_{\rm K} \to 0$: $W \sim \exp[-1.4\Delta/(eaE_{\rm AC})]$ (see Supporting Information), which showcases the exponential dependence on the external electric field characteristic of the nonperturbative tunneling processes such as (static) Schwinger effect [cf. eq 1]. The corresponding Schwinger field is $1.4\Delta/(ea)$, where the prefactor 1.4 is specific for MAPbBr3. In the multiphoton absorption regime, $W \sim (E_{\rm AC})^{2\Delta/\omega}$. Note that pure adiabatic tunneling competes with the avalanche breakdown. Indeed, the condition $\omega \gtrsim eE_{\rm AC}/\sqrt{m\Delta} \simeq eaE_{\rm AC}/\hbar$ is clearly violated in the limit $\gamma_{\rm K} \to 0$. Therefore, in what follows, we focus on quasiadiabatic tunneling with $\gamma_{\rm K} \simeq 1$.

For the experimental data presented in Figure 1D, $E_{\rm AC}$ is in between 0.24 and 0.36 V/a (which corresponds to $E_{\rm AC} \simeq 0.1\Delta/(ea)$). For that data $\hbar\omega \simeq 0.3$ eV, so that $\gamma_{\rm K} \simeq 1$. This puts the experiment in the quasi-adiabatic tunneling regime, i.e., the regime that extrapolates between eq 1 and multiphoton absorption. As we argue below, the data in Figure 1D is described quantitatively well using eq 2 with the parameters of MAPbBr₃. It is worth noting that we work with fields much smaller than the Schwinger field for our system. Nevertheless, we observe the PL signal in particular because we are in a quasi-adiabatic regime, where the nonzero frequency of the laser reduces the field strength requirement.

Comparison to the Experiment. In this section we confirm the tunneling nature of the ionization by deriving the functional dependence of the PL intensity, $I_{\rm PL}$, on the strength of the pumping mid-infrared (mid-IR) radiation. Naively, one might assume $I_{\rm PL} \propto W$, i.e., every single tunneling event results in a PL photon. However, this is only true if: (1) there are no nonradiative recombination channels; (2) the photoexcited electron—hole pairs remain well-separated in space; (3) the density of charge carriers is low. Neither of these conditions are satisfied in our experiment. First of all, despite the excellent

photoelectronic properties of LHPs the nonradiative recombination processes in them cannot be ignored altogether. Similarly, the long diffusion lengths of photocarriers in LHPs imply strong overlap between electron—hole pairs, which gives rise to a bimolecular character of the recombination processes, see also Supporting Information for additional data in favor of a bimolecular character.

To quantitatively describe the photoluminescence in perovskites, one needs to know the population dynamics of photoexcitations n(t) from which one can calculate the PL intensity based upon the bimolecular recombination in lead halide perovskites, $I_{\rm PL} \sim \int_0^\infty n(t)^2 {\rm d}t$. The general equation governing the population of charge carriers n(t) can be written as

$$-dn(t)/dt = A_1 n + A_2 n^2 + A_3 n^3 + \dots$$
 (3)

Here, the coefficients $\{A_i\}$ describe the rates of different decay channels of n(t) such as defect-assisted (A_1) , bimolecular (both radiative- and nonradiative; A_2), and Auger-type (A_3) recombination processes followed by higher-order processes, which should, in principle, be taken into account for sufficiently high densities of charge carriers, see Figure 1E.

In the limit of weak pumping fields, n(t) remains small at all times, implying that $n(t) = n(0) \exp(-A_1 t)$ and $I_{\rm PL} \sim n(0)^2$ where the initial population n(0) is proportional to the tunneling ionization rate W. This result is accurate as long as $\ll A_1/A_2$. Note that $A_1/A_2 \simeq 3.5 \times 10^{16} \ {\rm cm}^{-3}.^{48}$ As the pumping intensity grows, the omission of higher-order terms in eq 3 is no longer justified. For example, the inclusion of both mono- and bimolecular channels leads to $I_{\rm PL} \sim \alpha W - \ln(1 + \alpha W)$, where α is a fitting parameter (see Methods). By fitting our data, we conclude that this expression is accurate for $E_{\rm AC} \lesssim 0.3 \ {\rm V/a}$, providing an estimate for a number of excited particles in the system $10^{16}-10^{17} \ {\rm cm}^{-3}$ at this field. For higher excitation densities, the channels beyond bimolecular recombination have to be included.

In Figure 1D we show the results of the fit limited to second (bimolecular) processes (yellow curve) as well a phenomenological fit including higher-order channels (red curve) line. The phenomenological fit is motivated by our analytical results. It has the form $I_{\rm PL} \sim \alpha \tilde{W} - \ln(1 + \alpha \tilde{W})$, where $\tilde{W} = W/(1 + \beta W)$ is a renormalized ionization rate that takes into account that for large densities only a fraction of charge carriers can recombine radiatively. Note that the phenomenological fit has now two parameters α and β . The overall prefactor that connects I_{PL} to n^2 is beyond the Landau-Dykhne approach. It can be treated as another fit parameter, which in a log-plot simply shifts the data along the vertical direction. Since the exact relationship between the total number of PL photons and the number of photons detected is generally unknown, the prefactor can be entirely omitted by properly normalizing the data, see Figure 1D.

■ APPLICATIONS OF TUNNELING IONIZATION

The hallmark feature of quantum tunneling is its exponential sensitivity to external parameters, which has enabled applications defying the classical common sense. The most celebrated example is the scanning tunneling microprobes where exponential sensitivity of the tunneling current means that the overwhelming majority of it is flowing through the single atom that happens to stick out the most toward the sample. ^{27,50} Realization of this has led to unprecedented

subatom-scale spatial resolutions. Other celebrated applications of tunneling-related process include the tunnel diode with its unique I-V characteristics and high-harmonic generation in atomic optics where deeply subthreshold laser light promotes electrons in an atom to unoccupied states, 52 thus initializing the process of extreme frequency conversion of radiation.

Likewise, besides being a fascinating example of quantum tunneling dynamics, our findings are also of practical importance. The inherent nonperturbative character of tunneling in our case leads to a possibility to amplify the effect of weak fields by driving the system with another laser field. The basic intuition here can be inferred already from the expression in eq 1, which suggests that the overwhelming majority of tunneling events occurs near the moment of time t_0 when the total field $E_{\text{tot}}(t)$ reaches its maximum $E_{\text{tot}}(t_0) = E_{\text{max}}$. For instance, in the case of tunneling under the simultaneous influence of two slowly changing electric fields $E_1(t) = E_1$ $\cos(\omega_1 t)$, and $E_2(t) = E_2 \cos(\omega_2 t + \phi)$, the total number of tunneling events according to this logic is expected to be N_{tun} = $\int W(t) dt \propto \exp(-E_s/(|E_1| + |E_2|))$ (see an illustration in Figure 2). While this simple example is valid only for $\omega_1, \omega_2 \rightarrow$ 0 it in fact illustrates the more general phenomenon of exponential cooperative enhancement of tunneling yield. A more rigorous treatment of this effect can be provided within

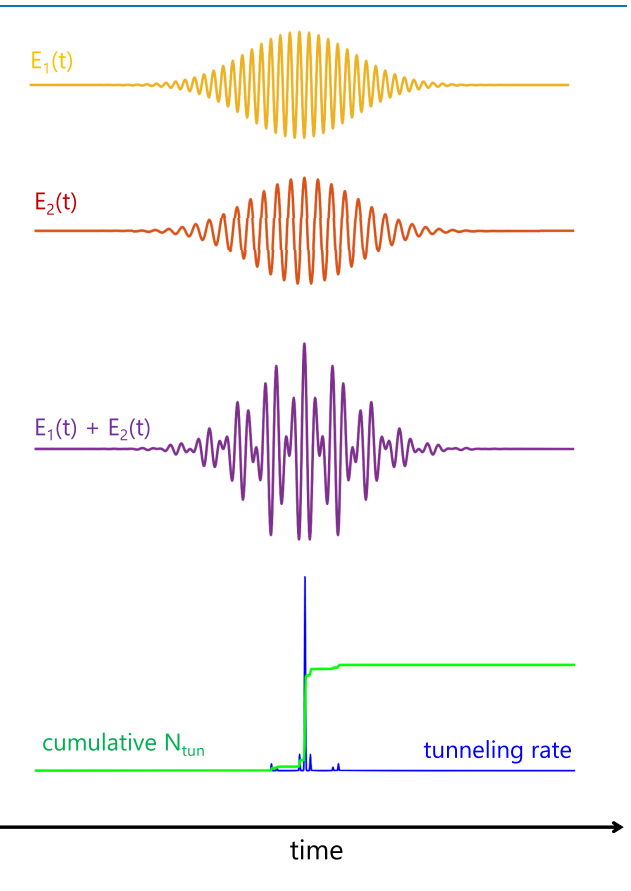


Figure 2. Sketch of tunneling under the influence of two slowly varying in time fields $E_1(t)$ and $E_2(t)$ (yellow and red curves at the top of the figure). Their sum $E_1(t) + E_2(t)$ is also presented (magenta). The tunneling rate (blue at the bottom of the figure) is exponentially enhanced at the maximum of the total field. Consequently the cumulatative number of transitions (green) is determined mainly by the value of this maximum.

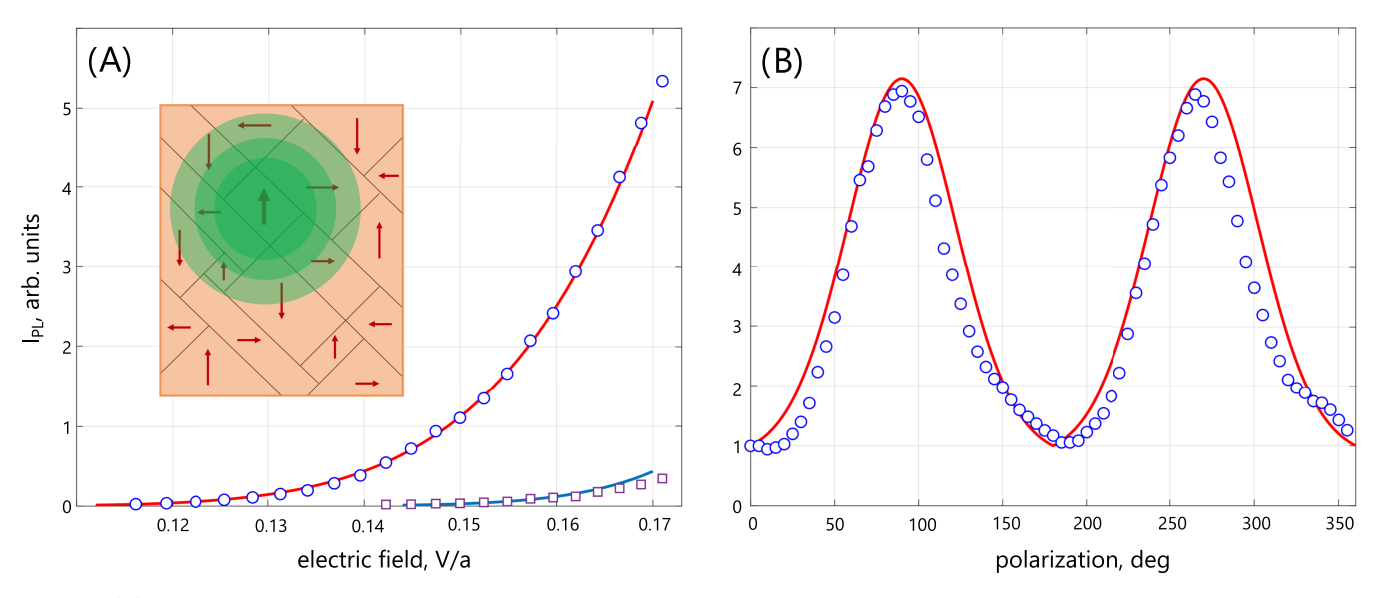


Figure 3. (A) PL as a function of the applied electric field for two orthogonal polarization orientations aligned with the crystal axes of MAPbBr₃ (markers). The corresponding fits according to our theoretical model to the data are presented as solid curves. The inset shows a cartoon of MAPbBr₃ with hypothetical ferroelectric domains overlaid with a schematic representation of the irradiating laser spot whose diameter is $d \approx 200 \, \mu \text{m} \, (1/e^2)$; (B) Polarization scan taken at a fixed value of the external electric field $E_{AC} \simeq 0.180 \, V/a$.

the quasi-adiabatic formalism.⁵³ Below, we illustrate that the exponential cooperative enhancement can indeed be used a valuable resource.

Detection of Polarization-Dependent Enhancement of Tunneling in LHP. The distinctive exponential sensitivity of tunneling ionization rate on the peak value of the *net* applied field can be used as a resource to detect weak local fields in a material. This can be best illustrated in the quasi-static regime describe above. Using the Landau-Dykhne approach it can also be demonstrated in a general case that even a weak static frozen-in field E_1 ($\omega_1=0$) can strongly enhance the tunneling rate W due to the additional driving field $E_2(t)$ (see Supporting Information). The fact that local fields can enhance PL yield is consistent with a qualitative observation that we see stronger PL in the vicinity of structural defects (edges, surfaces) of LHPs where internal electric fields, E_1 , are expected to appear. S4

As an application of this sensitivity of PL to E_1 we propose to use it to study the highly debated frozen-in electric fields E_{DC} in LHPs,⁵⁵ which lead to a broken inversion symmetry even for nominally cubic lead-halide perovskites. It is worth noting here that the method merits certain advantages as compared to some of the conventional techniques for detecting local breaking of inversion symmetry such as second-harmonic generation or angle-resolved photoemission. First of all, our method is not confined to the vicinity of the sample surface since the used electric fields have subgap frequencies and hence can penetrate the sample. Second, the peculiarity of tunneling is that it is sensitive to the absolute value of field amplitudes, cf. eq 1. Therefore, there is a finite net effect due to local inversion breaking even if the local fields spatially average to zero. Finally, another implication of the field cooperation is that PL should strongly depend on the polarization of the external field.

For experimental validation, we measure PL from a single-crystal MAPbBr₃ as a function of intensity of the driving midinfrared $\lambda = 4~\mu m$ radiation. The resulting dependence plotted in Figure 3A indicates that the tunneling ionization efficiency depends strongly on the polarization of the pumping field. To

elucidate the nature of this polarization dependence, we scan PL as a function of polarization at a fixed pump intensity as shown in Figure 3B.

The 2-fold symmetric polarization dependence in Figure 3B might appear surprising since this measurement was performed at room temperature where MAPbBr3 is expected to be in the cubic phase, i.e., 4-fold symmetric (e.g., consider the twophoton absorption experiments like in ref 56). The data in Figure 3B therefore indicates an unexpected lowering of symmetry in MAPbBr₃ in the nominally cubic phase. In the most straightforward explanation this could be attributed to an extrinsic factor such as residual stress in the crystal structure that would lift the 4-fold symmetry of the electronic band structure. However, it can be demonstrated that, that in this case in order to reproduce the magnitude of the effect in Figure 3 the intrinsic stains in the system have to reach relatively large (\$\sime\$ 0.5%) levels, \$\frac{57}{2}\$ which are not expected in a single-crystal LHP⁵⁸ (see Supporting Information for more details).

In an alternative scenario, the observed anisotropy can be attributed to the local frozen-in electric fields, that were conjectured to be present in lead-halide perovskites. 54,59 Indeed the exponential sensitivity of PL on applied fields implies that one can obtain the anisotropy observed in Figure 3 already with moderate static fields. In Figure 3A,B we show that all of the experimental data can be reproduced within the two-field Landau-Dykhne formalism presented in the Supporting Information. Based on the fitting, we estimate the numeric value for the internal static fields in room-temperature singlecrystal MAPbBr₃ to be of the order of $E_{\rm DC} \sim 0.1 \ {\rm V/nm}$. Within this interpretation of the PL anisotropy, the PL gets maximum enhancement when the polarization of the driving optical field coincides with the direction of E_{DC} . That this direction happens to be aligned with direction of Pb-Br bonds ([001] of the cubic lattice) is consistent with previous observations of possible ferroelectricity in MAPbI₃. One that Figure 1D is produced using electric fields that are stronger than those presented in Figure 3A. Further, we rotated the polarization of the external electric field to have minimal PL intensity. This

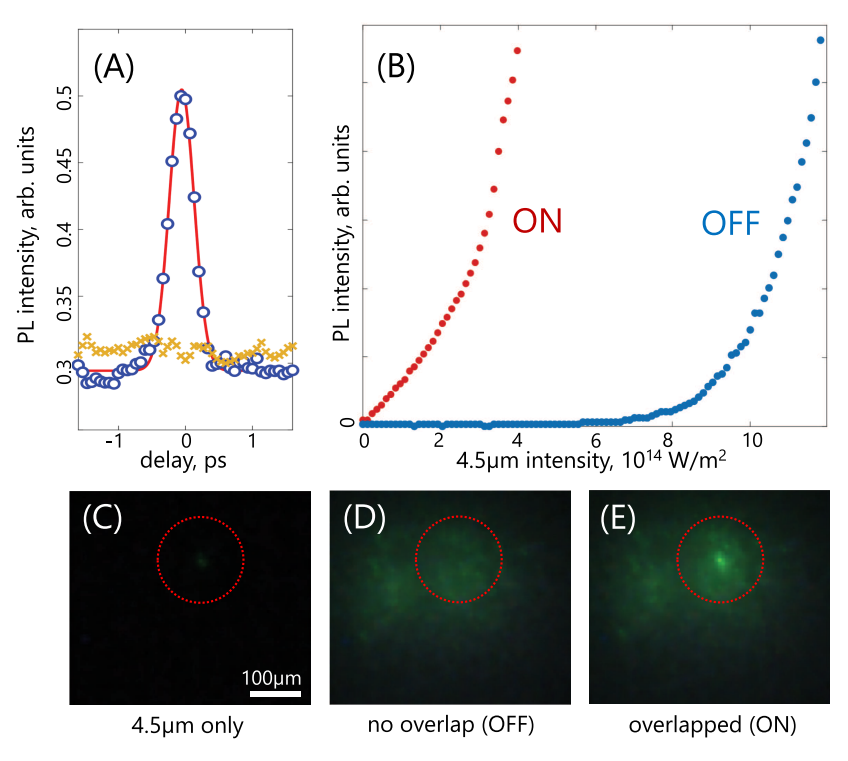


Figure 4. (A) Cumulative PL from a single-crystal sample MAPbBr₃ as a function of the time delay between 1 and 4 μ m pulses with parallel- (blue circles) and orthogonal (yellow crosses) polarizations; solid red line is a Gaussian fit to the curve used as the guide to an eye; (B) Differential PL from a single-crystal sample MAPbBr₃ as a function of mid-infrared intensity (4.5 μ m) biased with 1 μ m at $I_{bias} = 5 \times 10^{13}$ W/m² (mid- and near-infrared pulses overlap in time; red points) as compared to PL induced by the same mid-infrared beam in the absence of AC-biasing (mid- and near-infrared pulses do not overlap in time; black points). Panels (C–E) demonstrate spatial profiles of PL under AC-biasing in an abraded sample of MAPbBr₃. Namely, panel (C) shows PL produced by the pulse 4.5 μ m alone; panels (D) and (E) present spatial profiles of cumulative PL with 1 and 4.5 μ m pulses not overlapped and overlapped in time, respectively. The red circle in (C–E) marks the position of and the spot size (1/e²) of the 4.5 μ m light beam.

allowed us to minimize the effect of the frozen-in electric fields in the data demonstrated in Figure 1D.

Importantly, we also observe that the 2-fold symmetric pattern of PL is subject to the spatial extent of the focal spot of the driving laser. Namely, we observe that the 2-fold symmetry in Figure 3 is only present for sufficiently focused beams. For larger illumination spots, the pattern turns out to be 4-fold symmetric (see Supporting Information). This can be naturally explained if more than one ferroelectric domain with different field directions participate in the fluorescence process. This interpretation agrees well with the previous estimations of the size of possible ferroelectric domains of several microns in MAPbI₃, ^{59,62}

Cooperation of Dynamic Fields and AC-Biasing. The cooperation effect illustrated in Figure 2 implies that the total yield of tunneling ionization across the band gap driven by an AC-field can be significantly enhanced in the presence of an additional "boosting" AC-field, which does not have to be in any particular phase or frequency relationship to the first field. In order to demonstrate this "AC-biasing" phenomenon, we measure the PL from the MAPbBr₃ sample irradiated by a 4.5 μ m beam while it is being "AC-biased" by an additional 1 μ m beam, see Experimental section for details.

In Figure 4A we show the cumulative PL, $\int_{-\infty}^{\infty} \mathrm{d}t I_{\mathrm{PL}}(t,\tau)$, coming from the sample as a function of the delay time (τ) between the two pulses in cross- and parallel polarization geometries (yellow x- and blue o-markers, respectively). As can be clearly seen, the PL signal is enhanced only when the two pulses of the same polarization overlap in time, i.e., when the

amplitude of the sum field is maximized in full qualitative agreement with the concept of the dynamical assistance in quantum tunneling introduced in the previous sections.

As a demonstration of the practical use of this effect, we present in Figure 4B the effect of AC-biasing on PL produced by a mid-infrared beam (4.5 μ m) in MAPbBr₃ biased with 1 μ m radiation at $I_{\rm bias}=5\times10^{13}$ W/m², see Supporting Information for additional data. Here, we show the differential photoluminescence for two beams $\Delta {\rm PL}(I)={\rm PL}(I_1,\,I_{\rm bias})-{\rm PL}(I_1,\,0)-{\rm PL}(0,\,I_{\rm bias})$, where PL($I_1,\,I_{\rm bias})$ stands for the total PL emitted by the sample when irradiated by mid- and near-infrared pulses overlapping in time. As can be seen the differential sensitivity of PL can be made linear in the intensity of the mid-IR which opens broad possibilities for efficient mid-infrared sensors based upon lead-halide perovskites.

There is a caveat to consider when designing such a sensor. All the results presented thus far correspond to measurements on a single crystal, away from any structural features like crystal edges. This approach was taken because, as demonstrated above, the efficiency of tunneling ionization is highly sensitive to the local properties of the sample (e.g., stress, static fields). For instance, we observe that photoluminescence (PL) becomes visibly enhanced when the irradiated region is near structural defects such as surface inhomogeneities or sample edges/cracks. This is problematic for potential infrared imaging applications, as structure-induced variations in PL may obscure the actual spatial distribution of the mid-infrared wavefront we aim to probe.

Figure 5. Experimental setup for probing the AC-biasing effect. The output of a near-infrared (NIR) pulsed laser is used to pump an optical parametric amplifier (OPA) that generates tunable mid-infrared (MIR) radiation. The MIR intensity is controlled using a pair of wire-grid polarizers. A small fraction (\sim 5%) of the original NIR beam is split off using a beamsplitter to provide the AC biasing. A motorized delay stage controls the relative timing between the NIR and MIR pulses. The intensity of the biasing NIR beam is adjusted using a combination of a half-wave plate and two polarizers. The NIR and MIR beams are then combined using a dichroic mirror and focused onto the sample. The resulting photoluminescence (PL) is collected and measured using an amplified silicon photodiode after filtering out the NIR and MIR pump beams.

Sample imperfections are unavoidable in practice. Therefore, not being able to ensure sample homogeneity by removing the imperfections one can take the other extreme and instead homogenize the defect distribution, thus obtaining a quasiuniform sample suitable for infrared-imaging purposes. To demonstrate this approach in practice, we deal with abraded powder samples (see Supporting Information). Although, the intrinsic in-homogeneity of these samples does not allow for a quantitative description, they can be directly used for sensing as we demonstrate by overlapping the two beams (mid- and near-infrared) on a screen covered by the abraded sample. As can be seen in Figure 4C-E, there is clear enhancement in local PL from the region of spatial overlap. Curiously, due to the nonlinear sensitivity of PL on the pumping beam intensity, the apparent size of the overlap spot is significantly smaller (11 μ m) than the actual spot size of the mid-infrared pulse (160 μ m), which can be employed for super-resolution microscopy.

SUMMARY

To summarize, we have demonstrated tunneling ionization in a Dirac semiconductor, quantitatively described it with the quasi-adiabatic Landau-Dykhne approach, and interpreted it in terms of analogue dynamical Schwinger effect. This became possible due to unique photoelectric properties of lead halide perovskites, particularly due to their very high quantum PL efficiency, which enables a detection of tunneling-ionized carriers through PL long before impact ionization becomes relevant. Furthermore, a considerable energy gap of MAPbBr₃ allowed us to easily rule out all upconversion mechanisms based upon low energy scales of the material, for example, a phonon-assisted upconversion. ^{63,64} Indeed, one would require of the order of 50 phonons to account for a difference between the frequencies of the driving field and the PL signal.

Utilizing the exponential sensitivity of tunneling ionization to driving fields, we measured the polarization dependence of the PL signal and interpreted the results by invoking local frozen-in fields in a nominally cubic MAPbBr₃ single crystal at room temperature. These results provide new insights into the ongoing debate on polar order in lead-halide perovskites. Finally, we have investigated the cooperation between two time-dependent fields simultaneously driving tunneling ionization and demonstrated that this cooperation can act as an AC analogue of biasing for an optical frequency (nonparametric) upconversion. These findings pave the way for a mid-infrared light detection with lead-halide perovskites.

■ EXPERIMENTAL SECTION/METHODS

Experimental Setup. The experimental setup, see Figure 5, consisted of an amplified femtosecond laser system (Light Conversion PHAROS) coupled to an optical parametric amplifier (OPA, Light Conversion ORPHEUS). The laser produces a train of pulses centered at 1028 nm with a repetition rate of 3 kHz, pulse duration of 300 fs and a pulse energy of 2 mJ. A small fraction (5%) of the main beam was split off and used as a NIR probe while the main part pumped the OPA producing a MIR pump beam. Pump and probe pulses were spatially and temporally overlapped inside the LHPs. The resulting PL was sampled with an amplified silicon photodetector (PDA-100A2, Thorlabs). A short pass filter (Thorlabs) was used in order to cut off the remaining 1030 nm light.

The PL spectra were taken in reflection geometry by pumping the sample with respective wavelengths at an intensity of $1 \times 10^{11} \text{ W/cm}^2$ and sampling the PL with a fiber coupled spectrometer (OceanOptics FLAME-T).

The beam diameters were characterized for both the MIR and NIR beams. For the former we employed the knife edge technique, ⁶⁵ while for the latter a direct imaging by a CMOS camera has been applied. In Figure 6, we illustrate the knife-edge data for the pump wavelength of 4 μ m. It corresponds to the measurement reported in Figure 1 of the dependence of PL intensity on the magnitude of the external laser field.

Similarly in the two-color experiment (see Figure 4) that was performed by mixing the 1 and 4 μ m fields, we characterized the spot size of the latter by the knife-edge technique while for the former we used a direct imaging by a CMOS camera. We extracted a beam radius of 113 μ m for the MIR beam and a transverse radius of 83 μ m \times 121 μ m for the elliptical NIR beam, see Figure 7. Note that we used spatial filtering in the MIR arm and hence the beam was almost perfectly radially symmetric in this case.

Polarization resolved scans were performed by first converting the linearly polarized MIR radiation from the OPA into a circularly polarized state by means of a tunable quarter-wave plate (ALPHALAS) and a subsequent rotation of the polarization plane by a wiregrid polarizer (THORLABS).

In the two-color experiment a pair of half-wave plate and Glan-Taylor polarizer (GT10, Thorlabs) and a pair of wiregrid polarizers were used to continuously tune the incident power in the 1030 and 4500 nm arms, respectively. For imaging the $MAPbBr_3$ sample was placed in a defocused 1030 nm beam while being kept in the focus of the 4500 nm pump beam. The

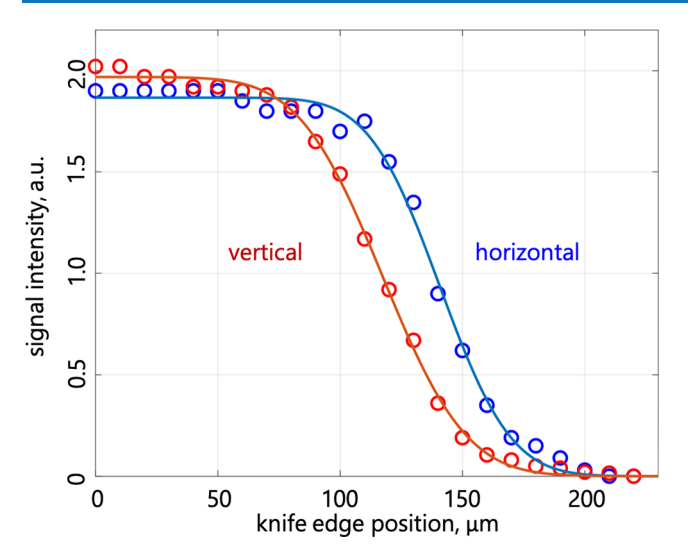


Figure 6. 4 μ m pump beam spot size as characterized by the knife-edge technique. The blue circles correspond to the scan in the horizontal plane while the yellow circles mark the scan in the vertical plane. From the latter we extracted the beam radii of 44 and 53 μ m, respectively. These values were subsequently used to evaluate the peak intensity and analyze the data presented in Figure 1.

images were then taken using a CMOS camera (Point Gray Research PGR-CM3-U3-50S5M-CS).

Calculation of Photoluminescence. To understand the parametric dependence of the PL, we use the Landau-Dykhne adiabatic approximation where the probability of transition from the initial state i to the final state f is given by the expression $(\hbar = 1)^{45}$

$$W_{fi} \sim \exp\left(-2\operatorname{Im}\int_{0}^{T} \left(\mathcal{E}_{f}(t) - \mathcal{E}_{i}(t)\right) dt\right)$$
 (4)

where $\mathcal{E}(t)$ is the instantaneous energy of the time-dependent Hamiltonian, H; T is the (complex) instance of time when $\mathcal{E}_f(t)=\mathcal{E}_i(t)$. To calculate the energies, we use the following Hamiltonian^{29,34}

$$H = \frac{1}{2} \left(\Delta + t_3 \frac{(\mathbf{k}a)^2}{2} \right) \tau_3 \otimes \sigma_0 + 2ta\tau_2 \otimes \sum_{l=1}^3 \sigma_l k_l \tag{5}$$

which describes the band structure in the vicinity of the bandgap, i.e., $k \to 0$. Here, $\Delta \simeq 2.4$ eV is the energy gap between the conduction and valence bands; $t \simeq 0.6$ eV and t_3 $\simeq 0.9$ eV are the hopping integrals; $a \simeq 0.586$ nm is the lattice spacing; τ_i and σ_i are the Pauli matrices acting on the orbital and quasispin degrees of freedom, respectively. Further details of the used notation can be found in ref 35. Note that we do not include the spin-electric term³⁶ in our calculations, because its contribution will be subleading for $\omega \to 0$ (see Supporting Information). External fields enter eq 5 via the minimal coupling substitution $k \rightarrow k - eA$; we shall assume weak fields so that $eaA \rightarrow 0$. We are interested in the regime that is exponentially sensitive to the parameters. Therefore, we shall consider k = 0, which determines the most probable excitation process. With these approximations, the Hamiltonian of interest reads

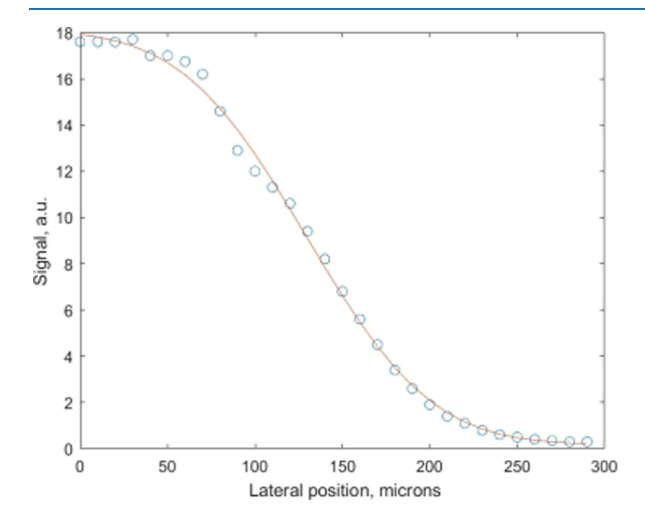
$$H = \frac{1}{2} \left(\Delta + \frac{t_3 (ea\mathbf{A})^2}{2} \right) \tau_3 \otimes \sigma_0 + 2eat\tau_2 \otimes \sum_{l=1}^3 \sigma_l A_l$$
 (6)

Its energies are

$$\mathcal{E}_{i} = -\sqrt{\frac{1}{4} \left(\Delta + \frac{t_{3} (ea\mathbf{A})^{2}}{2} \right)^{2} + 4t^{2} (ea\mathbf{A})^{2}}$$
 (7)

and $\mathcal{E}_f = -\mathcal{E}_i$. Note that the energy states are double degenerate. Therefore, in general, we should define a conserved quantity—quasi-spin, and consider separate quasi-spins in parallel. However, as eq 4 is independent of this quantum number, we will not take this degeneracy into account. To calculate the value of τ that appears in eq 4, we solve the equation $\mathcal{E}_i = 0$, which leads to $(ea\mathbf{A})^2 \simeq -\Delta^2/(\Delta t_3 + 16t^2)$. This expression together with eqs 4 and 7 provide the basis for our calculations of PL in the main text.

As an example, let us calculate the PL intensity for a monocromatic light beam. We assume that the vector potential has the form $\mathbf{A} = -\mathbf{E}_{AC} \sin(\omega t)/\omega$, where \mathbf{E}_{AC} is a constant



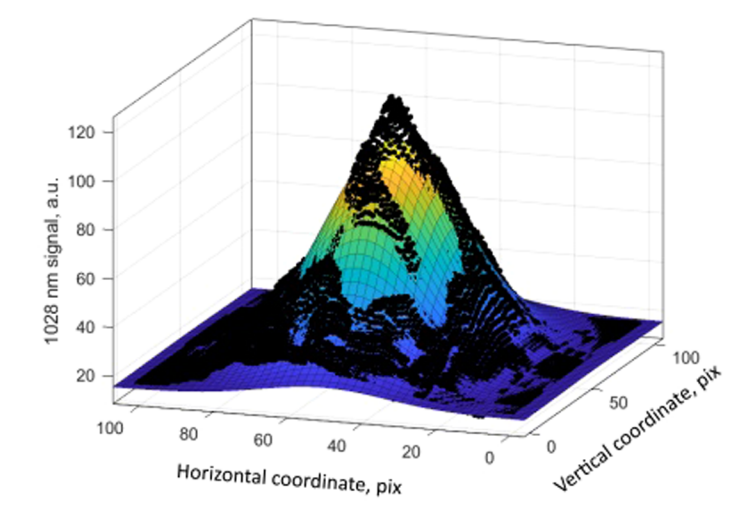


Figure 7. 4.5 μ m pump beam spot size as characterized by the knife-edge technique (left) and the 1 μ m beam spot as imaged by a CMOS camera (right), see the text for more details.

vector that defines the strength of the electric fields (recall that $\mathbf{E} = -\partial \mathbf{A}/\partial t$ in SI units). It is clear that to satisfy $\mathcal{E}_f(t) = \mathcal{E}_i(t)$, t should be imaginary, i.e., $t = i\tau$, where

$$\tau = \frac{1}{\omega} \operatorname{arsinh} \left(\frac{\omega}{eaE_{AC}} \sqrt{\frac{\Delta^2}{\Delta t_3 + 16t^2}} \right)$$
 (8)

Now, we have all ingredients to calculate W_{fi}

$$W_{fi} \sim \exp\Biggl(-2 \mathrm{Im} \int_0^{i au} \Biggl[\Delta + \dfrac{\Delta t_3 + 16t^2}{2\Delta} (\mathbf{eaA})^2\Biggr] \mathrm{d}t\Biggr)$$

which leads to eq 2 of the main text with the Keldysh parameter for our problem

$$\gamma_{\rm K} = \frac{\omega}{eaE_{\rm AC}} \sqrt{\frac{\Delta^2}{\Delta t_3 + 16t^2}} \tag{9}$$

PL Intensity at Strong Fields. Let us first consider the situation when $n_0 = n(0)$ is of the order of A_1/A_2 , but still much smaller than $A_2/A_3 \simeq 10^{18}$ cm⁻³.⁴⁸ In this case $dn/dt = -A_1n - A_2n^2$, which leads to $n = Ce^{-A_1t}/(1 - A_2 Ce^{-A_1t}/A_1)$, where $C = n_0/(1 + A_2n_0/A_1)$. The corresponding PL intensity reads

$$I_{\rm PL} \sim \left(n_0 + \frac{A_1}{A_2} \ln \left[\frac{A_1}{A_1 + A_2 n_0} \right] \right)$$
 (10)

Noticing that $W_{fi} \sim n_0$, we recover the result presented in the main text: $I_{\rm PL} \sim \alpha W_{fi} - \ln(1+\alpha W_{fi})$, where α is a fitting parameter. Inclusion of the processes with i>2 in the rate equation will lead to more fitting parameters, and, correspondingly, to a better agreement between the theory and the data. From a physical point of view higher-order processes suppress two-body losses, and effectively renormalize the initial density for the radiative recombination. Phenomenologically, this can be easily included using the following expression $I_{\rm PL} \sim \frac{\alpha W_{\rm fi}}{1+\beta W_{\rm fi}} - \ln \left(1+\frac{\alpha W_{\rm fi}}{1+\beta W_{\rm fi}}\right)$. This expression with the fitting parameters α and β reproduces our data well everywhere.

ASSOCIATED CONTENT

Supporting Information

^{66,67} The Supporting Information is available free of charge at https://pubs.acs.org/doi/10.1021/acsphotonics.5c01360.

Sample preparation; numerical calculation of tunneling ionization; ionization in the presence of a frozen-in electric field; additional information in support of the bimolecular-recombination origin of photoluminescence; additional information for the discussion on frozen-in electric fields; hysteresis of photoluminescence intensity; abraded samples of MAPbBr₃; additional data for a two-color experiment; photoluminescence from CsPbBr₃. Supporting Information contains additional refs 66,67 (PDF)

AUTHOR INFORMATION

Corresponding Authors

Artem G. Volosniev – Department of Physics and Astronomy, Aarhus University, Aarhus DK-8000, Denmark; o orcid.org/0000-0003-0393-5525; Email: artem@phys.au.dk

Zhanybek Alpichshev — ISTA (Institute of Science and Technology Austria), Klosterneuburg 3400, Austria; Email: alpishev@ist.ac.at

Authors

Dusan Lorenc – ISTA (Institute of Science and Technology Austria), Klosterneuburg 3400, Austria

Ayan A. Zhumekenov — KAUST (King Abdullah University of Science and Technology), Thuwal 23955, Saudi Arabia; Present Address: School of Materials Science and Engineering (MSE), Nanyang Technological University, Singapore 639798; orcid.org/0000-0002-3216-5315

Seungho Lee – ISTA (Institute of Science and Technology Austria), Klosterneuburg 3400, Austria; ⊚ orcid.org/0000-0002-6962-8598

Maria Ibáñez – ISTA (Institute of Science and Technology Austria), Klosterneuburg 3400, Austria; ⊙ orcid.org/0000-0001-5013-2843

Osman M. Bakr — KAUST (King Abdullah University of Science and Technology), Thuwal 23955, Saudi Arabia; orcid.org/0000-0002-3428-1002

Mikhail Lemeshko – ISTA (Institute of Science and Technology Austria), Klosterneuburg 3400, Austria

Complete contact information is available at: https://pubs.acs.org/10.1021/acsphotonics.5c01360

Author Contributions

D.L. and A.G.V. contributed equally to this work.

The authors declare no competing financial interest.

ACKNOWLEDGMENTS

A.G.V. thanks Peter Balling for useful discussions. This research was supported by the Scientific Service Units (SSU) of ISTA through resources provided by the Electron Microscopy Facility (EMF), and by the Werner Siemens Foundation (WSS) for financial support.

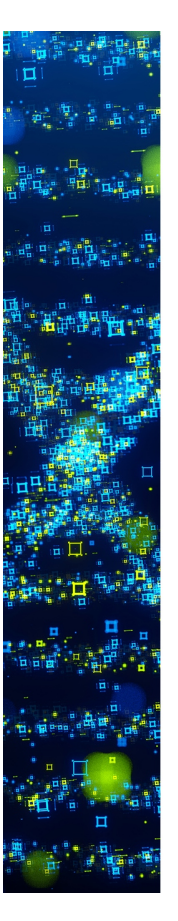
REFERENCES

- (1) Schwinger, J. On Gauge Invariance and Vacuum Polarization. *Phys. Rev.* **1951**, 82, No. 664.
- (2) Mourou, G. A.; Tajima, T.; Bulanov, S. V. Optics in the relativistic regime. *Rev. Mod. Phys.* 2006, 78, No. 309.
- (3) Brezin, E.; Itzykson, C. Pair Production in Vacuum by an Alternating Field. *Phys. Rev. D* **1970**, *2*, No. 1191.
- (4) Popov, V. S. Production of e^+e^- Pairs in an Alternating External Field. *J. Exp. Theor. Phys. Lett.* **1971**, 13, No. 195.
- (5) Ringwald, A. Pair production from vacuum at the focus of an X-ray free electron laser. *Phys. Lett. B* **2001**, *510*, 107–116.
- (6) Schützhold, R.; Gies, H.; Dunne, G. Dynamically Assisted Schwinger Mechanism. *Phys. Rev. Lett.* **2008**, *101*, No. 130404.
- (7) Gies, H.; Klingmüller, K. Pair production in inhomogeneous fields. *Phys. Rev. D* **2005**, 72, No. 065001.
- (8) Linder, M. F.; Schneider, C.; Sicking, J.; Szpak, N.; Schützhold, R. Pulse shape dependence in the dynamically assisted Sauter-Schwinger effect. *Phys. Rev. D* **2015**, *92*, No. 085009.
- (9) Torgrimsson, G.; Schneider, C.; Oertel, J.; Schützhold, R. Dynamically assisted Sauter-Schwinger effect non-perturbative versus perturbative aspects. *J. High Energy Phys.* **2017**, 2017, No. 43.
- (10) Szpak, N.; Schützhold, R. Optical lattice quantum simulator for quantum electrodynamics in strong external fields: spontaneous pair creation and the Sauter-Schwinger effect. *New J. Phys.* **2012**, *14*, No. 035001.

- (11) Kasper, V.; Hebenstreit, F.; Oberthaler, M.; Berges, J. Schwinger pair production with ultracold atoms. *Phys. Lett. B* **2016**, 760. 742–746.
- (12) Piñeiro, A. M.; Genkina, D.; Lu, M.; Spielman, I. B. Sauter-Schwinger effect with a quantum gas. *New J. Phys.* **2019**, *21*, No. 083035.
- (13) Zawadzki, W. Zitterbewegung and its effects on electrons in semiconductors. *Phys. Rev. B* **2005**, 72, No. 085217.
- (14) Allor, D.; Cohen, T. D.; McGady, D. A. Schwinger mechanism and graphene. *Phys. Rev. D* **2008**, *78*, No. 096009.
- (15) Fillion-Gourdeau, F.; MacLean, S. Time-dependent pair creation and the Schwinger mechanism in graphene. *Phys. Rev. B* **2015**, *92*, No. 035401.
- (16) Linder, M. F.; Lorke, A.; Schützhold, R. Analog Sauter-Schwinger effect in semiconductors for spacetime-dependent fields. *Phys. Rev. B* **2018**, *97*, No. 035203.
- (17) Sauter, F. Über das Verhalten eines Elektrons im homogenen elektrischen Feld nach der relativistischen Theorie Diracs. *Z. Phys.* 1931, 69, 742–764.
- (18) Zener, C. A theory of the electrical breakdown of solid dielectrics. *Proc. R. Soc. London, Ser. A* 1934, 145, 523–529.
- (19) Cohen, T. D.; McGady, D. A. Schwinger mechanism revisited. *Phys. Rev. D* **2008**, *78*, No. 036008.
- (20) Wehling, T.; Black-Schaffer, A.; Balatsky, A. Dirac materials. *Adv. Phys.* **2014**, *63*, 1–76.
- (21) Zawadzki, W. Semirelativity in semiconductors: a review. J. Phys.: Condens. Matter 2017, 29, No. 373004.
- (22) Jena, D. Quantum Physics of Semiconductor Materials and Devices; Oxford University Press, 2022.
- (23) Raizer, Y. P. Gas Discharge Physics; Springer: Berlin, Heidelberg, 1991.
- (24) Schmitt, A.; Vallet, P.; Mele, D.; Rosticher, M.; Taniguchi, T.; Watanabe, K.; Bocquillon, E.; Fève, G.; Berroir, J. M.; Voisin, C.; Cayssol, J.; Goerbig, M. O.; Troost, J.; Baudin, E.; Plaçais, B. Mesoscopic Klein-Schwinger effect in graphene. *Nat. Phys.* **2023**, *19*, 830–835.
- (25) Esaki, L. New Phenomenon in Narrow Germanium p-n Junctions. *Phys. Rev.* **1958**, 109, No. 603.
- (26) Giaever, I.; Megerle, K. Study of Superconductors by Electron Tunneling. *Phys. Rev.* **1961**, *122*, No. 1101.
- (27) Chen, C. J. Introduction to Scanning Tunneling Microscopy; Oxford University Press: Oxford, 2007.
- (28) Berdyugin, A. I.; Xin, N.; Gao, H.; et al. Out-of-equilibrium criticalities in graphene superlattices. *Science* **2022**, *375*, 430–433.
- (29) Jin, H.; Im, J.; Freeman, A. J. Topological insulator phase in halide perovskite structures. *Phys. Rev. B* **2012**, *86*, No. 121102.
- (30) Rethfeld, B.; Ivanov, D. S.; Garcia, M. E.; Anisimov, S. I. Modelling ultrafast laser ablation. *J. Phys. D: Appl. Phys.* **2017**, *50*, No. 193001
- (31) Braslavsky, S. E. Glossary of terms used in photochemistry, 3rd edition (IUPAC Recommendations 2006). *Pure Appl. Chem.* **2007**, 79, 293–465.
- (32) Kirchartz, T.; Márquez, J. A.; Stolterfoht, M.; Unold, T. Photoluminescence-Based Characterization of Halide Perovskites for Photovoltaics. *Adv. Energy Mater.* **2020**, *10*, No. 1904134.
- (33) Goetz, K. P.; Taylor, A. D.; Paulus, F.; Vaynzof, Y. Shining Light on the Photoluminescence Properties of Metal Halide Perovskites. *Adv. Funct. Mater.* **2020**, *30*, No. 1910004.
- (34) Becker, M. A.; Vaxenburg, R.; Nedelcu, G.; et al. Bright triplet excitons in caesium lead halide perovskites. *Nature* **2018**, *SS3*, 189–193.
- (35) Volosniev, A. G.; Kumar, A. S.; Lorenc, D.; Ashourishokri, Y.; Zhumekenov, A. A.; Bakr, O. M.; Lemeshko, M.; Alpichshev, Z. Effective model for studying optical properties of lead halide perovskites. *Phys. Rev. B* **2023**, *107*, No. 125201.
- (36) Volosniev, A. G.; Kumar, A. S.; Lorenc, D.; Ashourishokri, Y.; Zhumekenov, A. A.; Bakr, O. M.; Lemeshko, M.; Alpichshev, Z. Spin-Electric Coupling in Lead Halide Perovskites. *Phys. Rev. Lett.* **2023**, 130, No. 106901.

- (37) Zhang, Z.; Ning, H.; Liu, Z.-J.; Hou, J.; Mohite, A. D.; Baldini, E.; Gedik, N.; Nelson, K. A. Keldysh tuning of photoluminescence in a lead halide perovskite crystal. 2024. arXiv:2407.15253. arXiv.org e-Printarchive. https://doi.org/10.48550/arXiv.2407.15253.
- (38) Zhou, F.; Ran, X.; Fan, D.; Lu, S.; Ji, W. Perovskites: Multiphoton Absorption and Applications. *Adv. Opt. Mater.* **2021**, *9*, No. 2100292.
- (39) Mei, L.; Huang, R.; Shen, C.; Hu, J.; Wang, P.; Xu, Z.; Huang, Z.; Zhu, L. Hybrid Halide Perovskite-Based Near-Infrared Photodetectors and Imaging Arrays. *Adv. Opt. Mater.* **2022**, *10*, No. 2102656.
- (40) Jena, A. K.; Kulkarni, A.; Miyasaka, T. Halide Perovskite Photovoltaics: Background, Status, and Future Prospects. *Chem. Rev.* **2019**, *119*, 3036–3103.
- (41) Saidaminov, M. I.; Abdelhady, A. L.; Murali, B.; Alarousu, E.; Burlakov, V. M.; Peng, W.; Dursun, I.; Wang, L.; He, Y.; Maculan, G.; Goriely, A.; Wu, T.; Mohammed, O. F.; Bakr, O. M. High-quality bulk hybrid perovskite single crystals within minutes by inverse temperature crystallization. *Nat. Commun.* **2015**, *6*, No. 7586.
- (42) Tilchin, J.; Dirin, D. N.; Maikov, G. I.; Sashchiuk, A.; Kovalenko, M. V.; Lifshitz, E. Hydrogen-like Wannier-Mott Excitons in Single Crystal of Methylammonium Lead Bromide Perovskite. *ACS Nano* **2016**, *10*, 6363–6371.
- (43) Kruchinin, S. Y.; Krausz, F.; Yakovlev, V. S. Colloquium: Strong-field phenomena in periodic systems. *Rev. Mod. Phys.* **2018**, *90*, No. 021002.
- (44) Landau, L. D.; Lifshitz, E. M. Quantum Mechanics, 3 rd ed.; Butterworth-Heinemann, 1981.
- (45) Delone, N. B.; Krainov, V. P. Tunneling Ionization of Atom. In *Multiphoton Processes in Atoms*; Springer: Berlin Heidelberg, 2000; pp 69–83.
- (46) Keldysh, L. V. Ionization in the Field of a Strong Electromagnetic Wave. Sov. J. Exp. Theor. Phys. 1965, 20, 1307–1314.
- (47) Nathan, V.; Mitra, S. S.; Guenther, A. H. Review of multiphoton absorption in crystalline solids. *J. Opt. Soc. Am. B* 1985, 2, 294–316.
- (48) Richter, J. M.; Abdi-Jalebi, M.; Sadhanala, A.; Tabachnyk, M.; Rivett, J. P.; Pazos-Outón, L. M.; Gödel, K. C.; Price, M.; Deschler, F.; Friend, R. H. Enhancing photoluminescence yields in lead halide perovskites by photon recycling and light out-coupling. *Nat. Commun.* **2016**, *7*, No. 13941.
- (49) Stranks, S. D. Nonradiative Losses in Metal Halide Perovskites. *ACS Energy Lett.* **2017**, *2*, 1515–1525.
- (50) Binnig, G.; Rohrer, H.; Gerber, C.; Weibel, E. Surface Studies by Scanning Tunneling Microscopy. *Phys. Rev. Lett.* **1982**, 49, No. 57.
- (51) Electronics Engineer's Reference Book; Turner, L., Ed.; Elsevier, 1976.
- (52) Yue, L.; Gaarde, M. B. Introduction to theory of high-harmonic generation in solids: tutorial. *J. Opt. Soc. Am. B* **2022**, *39*, 535–555.
- (53) Perelomov, A. M.; Popov, V. S. Ionization of Atoms in an Alternating Electrical Field. III. *Sov. J. Exp. Theor. Phys.* **1967**, *24*, 309–326.
- (54) Niesner, D.; Wilhelm, M.; Levchuk, I.; Osvet, A.; Shrestha, S.; Batentschuk, M.; Brabec, C.; Fauster, T. Giant Rashba Splitting in CH₃NH₃PbBr₃ Organic-Inorganic Perovskite. *Phys. Rev. Lett.* **2016**, *117*, No. 126401.
- (55) Ambrosio, F.; Angelis, F. D.; Goñi, A. R. The Ferroelectric–Ferroelastic Debate about Metal Halide Perovskites. *J. Phys. Chem. Lett.* **2022**, *13*, 7731–7740.
- (56) Li, X.; Liu, W.; Song, Y.; Long, H.; Wang, K.; Wang, B.; Lu, P. Two-photon-pumped high-quality, single-mode vertical cavity lasing based on perovskite monocrystalline films. *Nano Energy* **2020**, *68*, No. 104334
- (57) Chen, Y.; Lei, Y.; Li, Y.; et al. Strain engineering and epitaxial stabilization of halide perovskites. *Nature* **2020**, *577*, 209–215.
- (58) Li, Y.; Tian, H.; Li, N.; Guo, J.; Ling, X.; Yuan, J.; Zhao, J.; Deng, Y. Long-Range Strain in Lead Halide Perovskite Single Crystals. *Cryst. Growth Des.* **2024**, *24*, 4473–4480.

- (59) Rakita, Y.; Bar-Elli, O.; Meirzadeh, E.; Kaslasi, H.; Peleg, Y.; Hodes, G.; Lubomirsky, I.; Oron, D.; Ehre, D.; Cahen, D. Tetragonal CH₃NH₃PbI₃ is ferroelectric. *Proc. Natl. Acad. Sci. U.S.A.* **2017**, *114*, E5504–E5512.
- (60) Röhm, H.; Leonhard, T.; Hoffmann, M. J.; Colsmann, A. Ferroelectric Poling of Methylammonium Lead Iodide Thin Films. *Adv. Funct. Mater.* **2020**, *30*, No. 1908657.
- (61) Leonhard, T.; Schulz, A. D.; Röhm, H.; Wagner, S.; Altermann, F. J.; Rheinheimer, W.; Hoffmann, M. J.; Colsmann, A. Probing the Microstructure of Methylammonium Lead Iodide Perovskite Solar Cells. *Energy Technol.* **2019**, *7*, No. 1800989.
- (62) Rothmann, M. U.; Li, W.; Zhu, Y.; Bach, U.; Spiccia, L.; Etheridge, J.; Cheng, Y.-B. Direct observation of intrinsic twin domains in tetragonal CH₃NH₃PbI₃. *Nat. Commun.* **2017**, 8, No. 14547.
- (63) Ye, Z.; Lin, X.; Wang, N.; Zhou, J.; Zhu, M.; Qin, H.; Peng, X. Phonon-assisted up-conversion photoluminescence of quantum dots. *Nat. Commun.* **2021**, *12*, No. 4283.
- (64) Dai, Y.; Qi, P.; Tao, G.; et al. Phonon-assisted upconversion in twisted two-dimensional semiconductors. *Light: Sci. Appl.* **2023**, *12*, No. 6.
- (65) Khosrofian, J. M.; Garetz, B. A. Measurement of a Gaussian laser beam diameter through the direct inversion of knife-edge data. *Appl. Opt.* **1983**, 22, 3406–3410.
- (66) Abiedh, K.; Zaaboub, Z.; Hassen, F. Mixed monomolecular and bimolecular-like recombination processes in CsPbBr₃ perovskite film revealed by time-resolved photoluminescence spectroscopy. *Appl. Phys. A* **2021**, *127*, No. 623.
- (67) Kumar, A. S.; Maslov, M.; Lemeshko, M.; Volosniev, A. G.; Alpichshev, Z. Massive Dirac-Pauli physics in lead-halide perovskites. *npj Quantum Mater.* **2025**, *10*, No. 37.



CAS BIOFINDER DISCOVERY PLATFORM™

STOP DIGGING THROUGH DATA —START MAKING DISCOVERIES

CAS BioFinder helps you find the right biological insights in seconds

Start your search

